ADVANCED FUNCTIONAL MATERIALS
www.afm-journal.de

# Design Principles of Diketopyrrolopyrrole-Thienopyrrolodione Acceptor$_1$–Acceptor$_2$ Copolymers

*Andreas Erhardt, Julian Hungenberg, Paul Chantler, Meike Kuhn, Thanh Tung Huynh, Adrian Hochgesang, Mahima Goel, Christian J. Müller, Subhayan Roychoudhury, Lars Thomsen, Nikhil V. Medhekar, Eva M. Herzig, David Prendergast, Mukundan Thelakkat,* and Christopher R. McNeill**

**The design principles of acceptor$_1$–acceptor$_2$ copolymers featuring alternating diketopyrrolopyrrole (DPP) and thienopyrrolodione (TPD) moieties are investigated. The investigated series of polymers is obtained by varying the aromatic linker between the two acceptor motifs between thiophene, thiazole, pyridine, and benzene. High electron affinities between 3.96 and 4.42 eV, facilitated by the synergy of the acceptor motifs are determined with optical gaps between 1.37 and 2.02 eV. Grazing incidence wide-angle X-ray scattering studies reveal a range of film morphologies after thermal annealing, including face-on, end-on and superstructure edge-on-like crystallites. Conversely, all materials form thin edge-on layers on the polymer–air interface, as demonstrated by multi-elemental near-edge X-ray absorption fine-structure spectroscopy. The benefit of the electron-deficient linkers thiazole and pyridine is evident: In organic field effect transistors, electron mobilities of up to $4.6 \times 10^{-2}$ cm$^2$ V$^{-1}$ s$^{-1}$ are obtained with outstanding on/off current ratios of $5 \times 10^5$, facilitated by the absence of detectable hole transport in these materials. Viability for all-polymer solar cells is assessed in active layer blends with the donor polymer PM6, yielding a maximum average power conversion efficiency of 4.8% and an open circuit voltage above 1 V.**

## 1. Introduction

The discovery of organic semiconductors sparked efforts to find hydrocarbon-based materials with optoelectronic properties similar to traditional inorganic semiconductors.[1] The first developments of materials, either small molecule or polymer-based, were motivated by the fabrication of low-cost and flexible organic light-emitting diodes, which finally yielded materials suitable for technology.[2,3] Further developments in the field were driven by organic photovoltaic (OPV) applications with the goal of fabricating efficient thin film OPV devices via printing and other non-conventional processing methods.[4] Recently, further applications such as organic electrochemical transistors for bioelectronic interfacing using mixed conductors or organic/hybrid thermoelectric for energy conversion have become the focus of research.[5,6] While material

A. Erhardt, J. Hungenberg, A. Hochgesang, M. Goel, C. J. Müller, M. Thelakkat
Applied Functional Polymers
University of Bayreuth
Universitätsstraße 30, 95447 Bayreuth, Germany
E-mail: mukundan.thelakkat@uni-bayreuth.de

A. Erhardt, P. Chantler, M. Kuhn, T. T. Huynh, N. V. Medhekar, C. R. McNeill
Department of Materials Science and Engineering
Monash University
Wellington Road, Clayton, Victoria 3800, Australia
E-mail: Christopher.McNeill@monash.edu

The ORCID identification number(s) for the author(s) of this article can be found under https://doi.org/10.1002/adfm.202314696



**DOI: 10.1002/adfm.202314696**

M. Kuhn, E. M. Herzig
Dynamics and Structure Formation – Herzig Group
University of Bayreuth
Universitätsstraße 30, 95447 Bayreuth, Germany

S. Roychoudhury, D. Prendergast
The Molecular Foundry
Lawrence Berkeley National Laboratory
1 Cyclotron Road, Berkeley, CA 94720, USA

L. Thomsen
Australian Synchrotron, ANSTO
Clayton, Victoria 3168, Australia

M. Thelakkat
Bavarian Polymer Institute (BPI)
University of Bayreuth
Universitätsstraße 30, 95447 Bayreuth, Germany

development for those fields and potential future applications heavily profit from the general knowledge gained from organic light emitting diode and OPV research, additional structure-property relation need to be established for understanding the optoelectronic functions and for designing more efficient materials, especially as acceptor systems. As an example, high-performance polymers for OPV applications are commonly equipped with hydrophobic alkyl substituents, while bioelectronics and thermoelectrics benefit from more hydrophilic side chains.[7,8] Further, cutting-edge materials are based on donor–acceptor (D-A) motifs, where electron-rich and electron-deficient monomers are copolymerized in an alternating sequence, leading to pronounced internal charge transfer characteristics ("push-pull effect").[9,10] The resulting polymers exhibit low optical bandgaps and high charge carrier mobilities, but display electron-donating characteristics in most cases, with only few exceptions. Acceptor polymers are often limited by their insufficient charge carrier mobility and operational stability in devices. A related design strategy, which is not as thoroughly studied lies in the class acceptor$_1$–acceptor$_2$ alternating copolymers. Linking two-different acceptor moieties has been shown to improve the coplanar backbone conformation and thus improved crystallinity and charge transport.[11] Here, the synergistic combination of several electron-deficient monomers leads to polymers with high electron affinity (low lying lowest unoccupied molecular orbital (LUMO) values), which leads to unipolar electron transport and is beneficial for the stability of the reduced state. Recent reports clearly show the viability of such design concepts for thermoelectric and organic electrochemical transistor (OECT) applications, as well as transport layers in perovskite solar cells.[12–14] The lack of high-performing acceptor polymers and the low amount of stable organic acceptor materials per se signifies the importance of a thorough evaluation of acceptor$_1$–acceptor$_2$ copolymers. A very interesting sub-field of organic photovoltaics is the field of all-polymer solar cells, employing active layers of polymer blends or single-component block copolymers with inherent advantage of morphological stability. However, in comparison to devices with small molecule acceptors (both fullerene and non-fullerene) in combination with donor polymers, lower power conversion efficiency (PCE) and higher operational stability can be observed in all-polymer solar cells. This tradeoff can be crucial for the establishment of OPV technology because the device lifetime and morphological stability of a blend is the Achilles heel of common organic technologies.

Previous studies from our group have demonstrated the suitability of a hydrophilic copolymer, based on diketopyrrolopyrrole (DPP: acceptor$_1$) and thienopyrrolodione (TPD: acceptor$_2$) for OECT and thermoelectric applications.[15,16] For a systematic structural variation, diverse aromatic carbonitrile educts can be employed during the synthesis of the DPP chromophore, which will later determine the aromatic linkers between the DPP and TPP units as we have demonstrated in an earlier D-A system.[17] Profound structural characterization has not been conducted yet for this recently successful new class of DPP-TPD-based copolymers.

In this study, we have synthesized a series of four hydrophobic DPP-TPD-based copolymers via direct arylation polymerization to investigate the influence of different aromatic flanking units systematically and thoroughly on structure formation and crystallite alignment. We correlate these nuanced structural changes to variations in the optoelectronic properties as well as thin film morphology and topography utilizing complementary methods including UV–vis absorption spectroscopy, cyclic voltammetry (CV), ultraviolet photoabsorption spectroscopy (UPS), organic field effect transistors (OFET), atomic force microscopy (AFM), grazing incidence wide-angle X-ray scattering (GIWAXS) and near edge X-ray absorption fine structure (NEXAFS) spectroscopy. Finally, the polymers were tested for their suitability as active acceptor components in binary all-polymer solar cells.

## 2. Results and Discussion

### 2.1. Polymer Design and Synthesis

The central design motifs of the series of acceptor$_1$–acceptor$_2$ copolymers used in this study are the electron-deficient repeating units, aryl flanked DPP and TPD, which were successfully incorporated individually into donor–acceptor copolymers in the past.[17–19] The aromatic flanking unit (Ar) of DPP was varied between different five- and six-membered moieties. Modifying this flanking unit was reported to influence the properties of D-A copolymers heavily.[20]

For the synthesis of the DPP monomers, known procedures were employed, starting with the respective aromatic carbonitriles of thiophene [T], thiazole [Tz], pyridine [Py], and benzene [Ph].[20,21] The latter two educts were brominated in the 4-position, as bromination at a later point is not feasible. The DPP monomers were attached with hexyl decyl branched N-substituents for guaranteeing sufficient solubility and brominated afterward, if necessary. The TPD unit was N-substituted with ethyl hexyl functionalities and used as the protonated monomer for direct arylation polymerization (DArP).[22] Microwave-assisted polymerization conditions were derived from our previous reports and the procedure from Leclerc et al., yielding the polymer series P1-[T], P2-[Tz], P3-[Py], and P4-[Ph] with the aromatic linker denoted in square brackets as shown in **Figure 1**.[15,16,23]

Detailed synthetic procedures for the monomers as well as the polymers are included in the ESI. All the spectroscopic and standard structural characterization are also provided in SI. After completion of the reaction, a color change is observable from a fluorescent pink, characteristic of the DPP monomers, to various shades of green, accompanied by an increased viscosity. Only the polymer with phenyl linkage remained pink and soluble in hexane. The GPC traces shown in Figure S1 (Supporting Information). confirm the formation of polymers with appreciably high molecular masses in the range of 26 to 56 kg/mol. The $M_n$ and dispersity values are listed in **Table 1**. After Soxhlet extraction, P1-[T] and P4-[Ph] show the presence of residual oligomers, whereas, P2-[Tz], P3-[Py] exhibit monomodal elution curves. Due to the presence of oligomers in the former, the $M_n$ values are comparatively smaller than for the latter. However, the molecular weights reported here are well above the effective conjugation lengths reported for conjugated polymers (≈10–12 repeating units) and therefore sufficient for comparative charge transport and structural studies. In a given structural motive, it has been earlier reported that the charge carrier mobility increases with

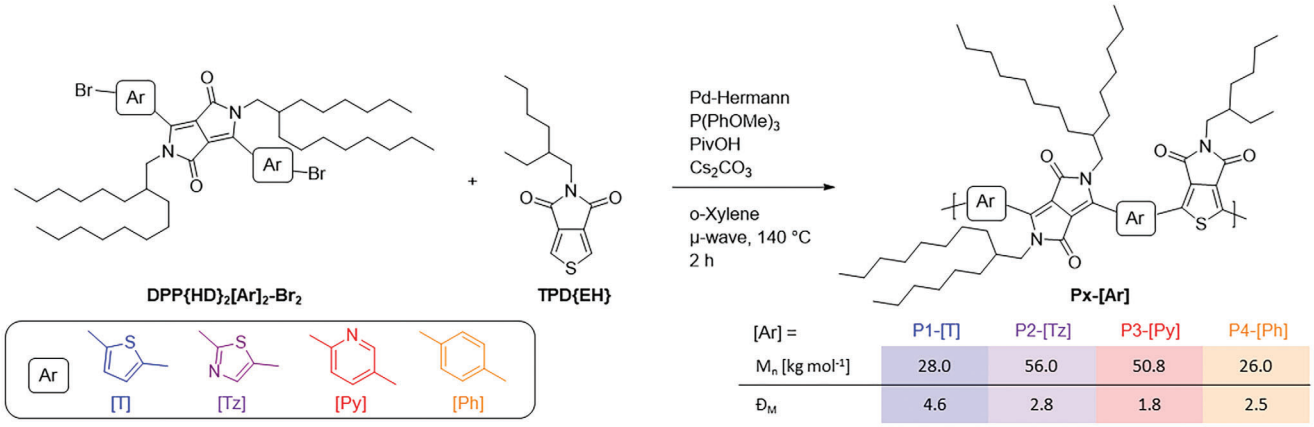


**Figure 1.** Synthesis of the acceptor$_1$–acceptor$_2$ type copolymers Px-[Ar] via microwave-assisted direct arylation polymerization, yielding materials with the molecular mass and dispersity listed on the right. [Ar] denotes the aromatic unit connecting the DPP and TPD motif.

molecular weight and saturates after specific molecular weight.[24] For example, in P3HT the properties saturate at an SEC molecular weight of 12 kD. Since all the polymers reported here have appreciably high molecular weights, we do not expect any significant influence of molecular weight on properties. Thermal stability with $T_{5\%}$ lying between 370 °C to 390 °C was determined via thermogravimetric analysis, as shown in Figure S2a (Supporting Information). No melting transitions were detectable via standard differential scanning calorimetry (cf. Figure S2b, Supporting Information). To increase the sensitivity of detection of thermal transitions, flash differential scanning calorimetry (DSC) analysis with heating rates up to 1000 K s$^{-1}$ was additionally conducted. The respective curves are depicted in Figure S3 (Supporting Information). Weakly pronounced melting and crystallization transitions could be clearly detected for samples, P1-[T] and P4-[Ph] and all the relevant data are summarized in Table 1.

### 2.2. Optoelectronic Properties

The thiophene linker is an electron-rich building block, while thiazole and pyridine exhibit a more electron-deficient nature.[25,26] Due to these different electronic properties of the polymer subunits and variations in non-covalent interactions, diverse optoelectronic polymer properties can be anticipated.

The UV–vis absorption spectra in thin film and solutions in 1,2-dichlorobenzene (1,2-DCB) depicted in **Figure 2a** showcase the significant influence of the DPP flanking units on the optical properties. The NIR absorption onset and maximum, observed in the P1-[T], experience a hypsochromic shift when the aromatic unit is replaced with the more electron-deficient thiazole- and pyridine linkers. A likely explanation lies in the relatively strong push-pull effect facilitated by the electron-rich thiophene unit, which decreases in strength for more electron-deficient units. The fact that a push-pull effect can be observed despite the combination of two acceptor building blocks in the system is due to the different electron affinity of the subunits.[27] Interestingly, in the polymers P1-[T], P2-[Tz], and P3-[Py], the predominant signal is the low energy peak, indicating an efficient $\pi$-conjugation between the DPP and TPD moieties via the flanking units along the polymer backbone.

Decisive for the extend of pi-conjugation and thus the UV–vis absorption of conjugated polymers is the planarity of the main-chain. To aid interpretation of the absorption properties, the dihedral angles of the polymers were calculated via DFT simlations (cf. Figures S4–S8, Supporting Information). As depicted in Figure 2d, P1-[T] and P2-[Tz] are close to perfect planarity with dihedral angles close to 0 ° or 180 ° between the respective five-membered linking units (thienyl or thiazolyl) and the adjacent DPP and TPD units. The low dihedral angles are reflected by the pronounced low energy signal in the absorption spectra, which is most likely associated to internal charge transfer processes. In contrast to P1-[T] and P2-[Tz], in the polymers P3-[Py] and P4-[Ph] six-membered rings are incorporated into the polymer main-chain. The dihetral angles are increased to 22.45 and 72.10° in P3-[Py] and 53.54 and 80.42° in P4-[Ph]. The substantial difference between these two polymers largely originates from the steric repulsion between the DPP N-substituent and phenyl proton in

**Table 1.** Thermal and optoelectronic material parameters of the synthesized acceptor$_1$–acceptor$_2$ copolymer series.

| Polymer | $M_n$ [kg mol$^{-1}$][a] | Đ[a] | $T_{5\%}$ [°C][b] | $T_m$ [°C][c] | $E_{g(opt)}$ [eV][d] | $IP_{UPS}$ [eV][e] | $EA_{CV}$ [eV][f] |
|---|---|---|---|---|---|---|---|
| P1-[T] | 28.0 | 4.6 | 409 | 377 | 1.37 | 5.39 | 4.27 |
| P2-[Tz] | 56.0 | 2.8 | 362 | 386 | 1.52 | 5.73 | 4.37 |
| P3-[Py] | 50.8 | 1.8 | 361 | 391 | 1.76 | 5.73 | 4.42 |
| P4-[Ph] | 26.0 | 2.5 | 413 | 373 | 2.02 | 5.94 | 3.96 |

[a] determined by GPC ($CHCl_3$, PS calibration); [b] determined by TGA ($N_2$, 10 K min$^{-1}$); [c] from flash DSC extrapolation of melting peaks to low heating rates; [d] determined via tauc-plot analysis from thin film UV–vis spectra; [e] determined via UPS; [f] extracted from CV (Thin film on ITO, DMF + 0.1 M TBABF).

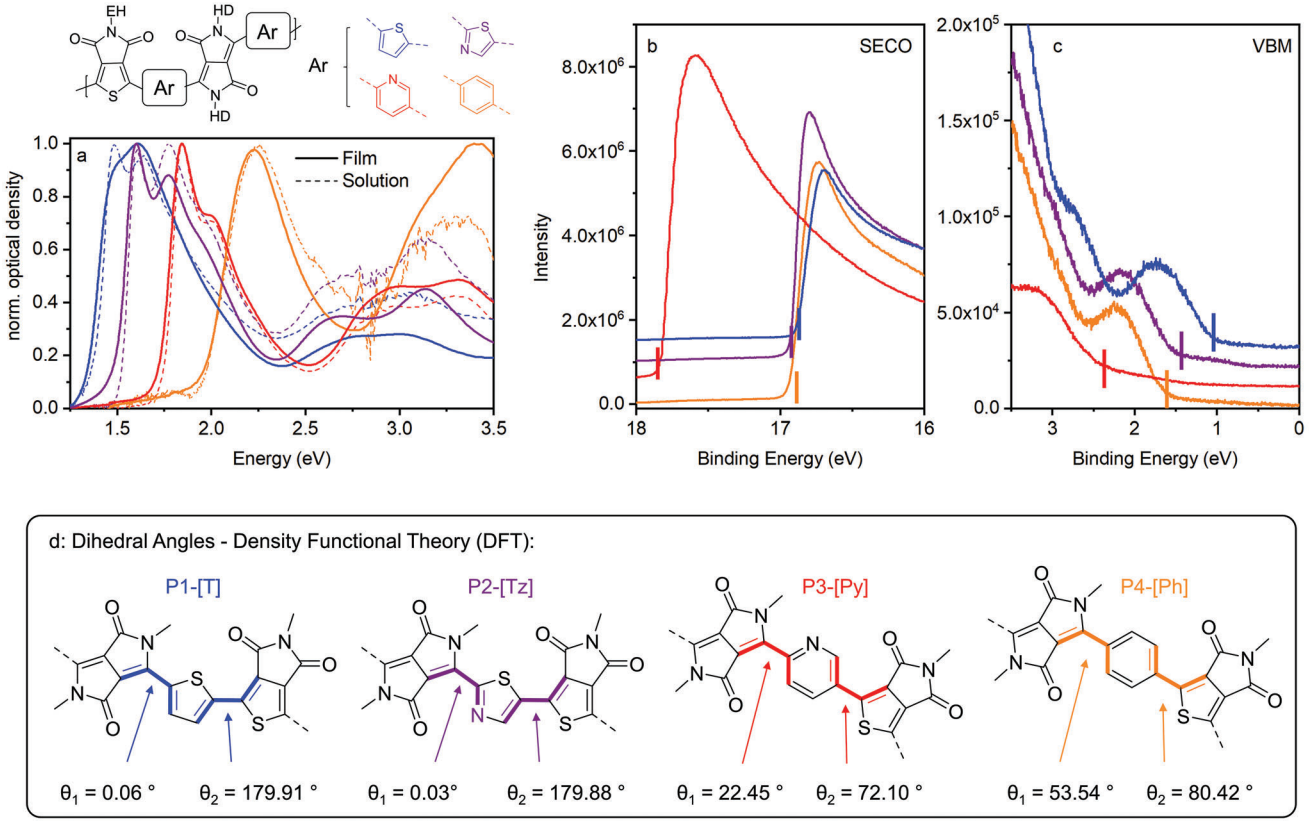


**Figure 2.** a) UV–vis absorption spectra recorded in as-cast films (solid lines) and 1,2-DCB solution (dashed lines) for the acceptor$_1$–acceptor$_2$ copolymers with the indicated aryl flanking units. b) SECO and c) VBM determined by UPS measurements of the polymer series. d) Dihredral angles between the aryl flanking units and the adjacent DPP and TPD moieties caluculated via DFT.

P4-[Ph], that is absent in P3-[Py]. This trend in dihedral angles is reflected in the blue shift of P3-[Py] compared to P2-[Tz] which is even more pronounced in P4-[Ph].

Low dihedral angles are further favored by attractive non-covalent forces between the DPP carbonyl oxygen, the thienyl and pyridyl proton, as well as the thiazolyl sulfur atom.[20,28]

It is worth acknowledging that the angle $\theta_2$ in P3-[Py] and P4-[Ph], deviates significantly from single crystal analysis of phenyl-substituted TPD, which can be considered a subunit of the polymer backbones. In single crystals, a dihedral angle of ≈27° is obtained, whereas the respective site in the DFT-calculated polymer chains exhibit angles above 70 °.[29] The reason for this deviation might be the simplified methyl N-substituents of the polyer structures that were conducted for DFT simulations, which may be correlated to the formation of helical superstrucutres in P3-[Py] and P4-[Ph] (cf. Figure S8, Supporting Information).

While the assignment of spectral signatures in the UV–vis spectra to the respective vibronic transitions is straight forward in established homopolymers like polythiophenes, peak interpretation is more complex for the copolymers shown here due to possible charge-transfer nature of transitions in addition to the $\pi$–$\pi^*$ transitions observed in homopolymers. In the case of homopolymers, e.g., polythiophene derivatives, the UV–vis main absorption spectra can be described as a superposition of a high-energy feature caused by disordered chains and a structured low-energy region caused by H-aggregated chains.[30] Following this interpretation, the absorption spectrum of the phenyl-linked polymer P4-[Ph] already differs considerably from the three other polymer systems by the absence of any vibronic fine structure of the low energy absorption region. The reason is an impeded aggregation of the polymer chain due to the high internal dihedral angle of ≈33° between the DPP core and the phenyl substituents.[20,31] In contrast, structured absorption features can be observed in the low energy spectral region of P1-[T], P2-[Tz], and P3-[Py] both in the polymer film and in 1,2-DCB solution (cf. Figure 2). According to Spano's model involving exciton-vibrational coupling in weakly interacting H-aggregates of conjugated polymers, the relative absorption intensity of the 0 → 0 transition compared to the 0 → 1 transition ($A_{0\text{-}0}/A_{0\text{-}1}$) is a measure of the coupling.[32] Aggregation can also be induced, and the nature of coupling can be studied by measuring UV–vis absorption by lowering the temperature of the solutions. Considering temperature-dependent UV–vis analysis, as seen in Figure S9 (Supporting Information), the influence on $A_{0\text{-}0}/A_{0\text{-}1}$ can be studied for the described copolymers. A decrease in temperature is clearly correlated to $A_{0\text{-}0}/A_{0\text{-}1}$ increase and hence an increase in order and decrease of the excitonic coupling. The thin film absorption spectra of P2-[Tz] and P3-[Py] accordingly exhibit pronounced 0-0 vibronic features. In contrast, the thin film absorption of P1-[T] shows broad peaks and does not resemble the solution spectra recorded at low temperature, hinting different modes of aggregation in film and solution.

The ionization potential (IP) of the polymers was determined via ultraviolet photoelectron spectroscopy (UPS), as depicted in Figure 2b. From the secondary electron cutoff (SECO) and valence band maximum (VBM) onset, the ionization potentials were calculated and listed in Table 1. The data for P3-[Py] is energetically offset compared to the remaining curves. Typically, such a shift is indicative of the n-doping of the material. However, we suspect an instrument shift occurred, as P3-[Py] was measured separately. Also, the OFET devices, discussed later, suggest the absence of any n-doping. The corresponding electron affinity values were determined via cyclic voltammetry as described in the experimental section (cf. Figure S10, Supporting Information). The EA of the phenyl-linked polymer P4-[Ph] differs from the remaining materials by ≈0.4 eV, in line with the previous observations.

### 2.3. Structural Investigation

Thin film microstructure is a fundamental property that significantly influences the charge transport properties of conjugated polymers.[33] Inconveniently, reliable predictions of crystallinity, structure, and texture are not possible, even though general correlations between molecular structure and microstructure were attempted in the past.[34] Therefore, exhaustive efforts to resolve the material morphology and topography are conducted here. All polymers are analyzed in the as-cast state after annealing for 90 minutes at 200 °C and after high-temperature annealing at 320 °C for 10 min (just below the TGA degradation onset) followed by slow cooling with a rate of 1 K $min^{-1}$. Characterization of as-cast films is representative of the processing conditions of organic photovoltaic bulk heterojunction layers, while the two annealing steps are employed to study the propensity of the materials to crystallize. Furthermore, high-temperature thermal treatments were recently reported to stabilize highly ordered polymer structures in a reproducible fashion.[35,36]

Upon comparison of the different copolymers, pronounced differences in the scattering patterns in **Figure 3**a–d are observable after high-temperature annealing. Likewise, the films show differences in the as-cast state and after annealing at 200 °C, which are less pronounced. The respective scattering patterns are included in Figure S11 (Supporting Information). The overall order increases upon annealing, recognizable by the increase of peak number and intensity and the decrease of peak width.[37] The as-cast films exhibit mostly isotropic features with weakly pronounced 100 and 010 peaks associated with lamellar and $\pi$–$\pi$ stacking, respectively. Upon annealing, additional peaks appear. The signals of the high-temperature annealed films can be assigned to crystallites with different unit cell parameters and surface-relative orientations ("textures"), as sketched in Figure 3e–h. For the samples P1-[T], P2-[Tz], and P3-[Py], a dominant face-on or end-on texture is found (*hkl* shown in white), respectively, with a minority edge-on phase (green annotation of *hkl*). The lattice dimensions of the two textures are identical in the thiazolyl and pyridyl-linked polymers and slightly distorted in the *b*-direction for the thienyl polymer (cf. **Table 2**). The correlation between molecular structure and crystallite orientation is an unanswered question up to date. The observed differences of the crystallite unit cells and textures can be caused by several factors. At least in the case of homopolymers (e.g., Polythiophenes), it has been proposed that two concurring processes – surface freezing and prefreezing – determine the final orientation. This is decided by the surface energy of the polymer as well as the nature of the substrate: In the case of acceptor-acceptor copolymers, such a study does not exist.[36] Substitution of the DPP flanking unit (hetero)atoms can lead to energetic inversion of the energetically favorable conformer and, therefore the linearity of the polymer chain. DFT calculations suggest such an inversion, e.g., when thiophene is replaced with thiazole in the copolymer PDPP-3T.[38] Further, the valence electron pair of nitrogen heteroatoms can form different intra- and intermolecular interactions than the methine group, influencing crystallinity and texture. In the case of the studied polymers, a contribution of both factors is likely. In the scattering image of P4-[Ph], amorphous features are seen, with a relatively low intensity of the crystalline peaks, indicative of a low degree of crystallinity in the material. This relatively low crystallinity, in turn, can be correlated to the high dihedral angle inferred by previous characterizations. Interestingly, the scattering pattern of the phenyl-linked material is highly atypical for conjugated polymers. The peak distance in the vertical direction fits the usual lamellar stacking distance of the other materials. However, no typical $\pi$–$\pi$ stacking peak is evident in the GIWAXS pattern of this material. Instead, peaks with a low $q$ spacing of approx. $\Delta q = 0.1$ Å$^{-1}$ are observable along a horizontal line at $q_z \approx 0.4$ Å$^{-1}$. The peaks can be indexed to match the crystallite parameters listed in Table 2, with the low $q$ separation corresponding to a spacing of 6 nm suggestive of a larger superstructure or supramolecular organization of chains. While the validity of peak indexing can be assumed to be sensible with high confidence, the respective real-space parameters are uncommon. We can exclude material degradation during high-temperature annealing as a reason for such patterns, as such peaks can already be observed when annealing is conducted at 200 °C (Figure S11h, Supporting Information). Instead, we suspect a high dihedral angle to increase the crystallographic repeating unit in the polymer backbone direction while weakening possible $\pi$–$\pi$- interactions. AFM provides further evidence for the existence of polymer superstructures (see below).

The penetration depth of GIWAXS can be controlled by variation of the incident angle, as visualized in Figure 3i. While shallow incident angles below the polymer critical angle $\alpha_c$ only probe the uppermost layer of the film (<10 nm), the bulk of the film is sampled just above the critical angle.[36] This correlation between incident angle and probing depth can be used to evaluate the crystallite structure- and orientation at different vertical positions in the film.

The quantification of different textural contents (e.g., amount of "face-on" vs "edge-on" crystallites) was conducted for different incident angles for the materials with thienyl-, thiazolyl-, and pyridyl- linkages (cf. Figure 3j). The minority phase, in the case of the presented films, consists of edge-on-aligned polymer crystallites. For this analysis, angular cuts, including the 100 signals of both crystal orientations, were conducted and angular corrected, as shown in Figure S12 (Supporting Information).[39] No such characterization was conducted for the phenyl-linked P4-Ph copolymer, as no 100 signal of a possible secondary texture was found. As shown in Figure 3j, the relative textural contents depend on the incident angle. Respective 2D

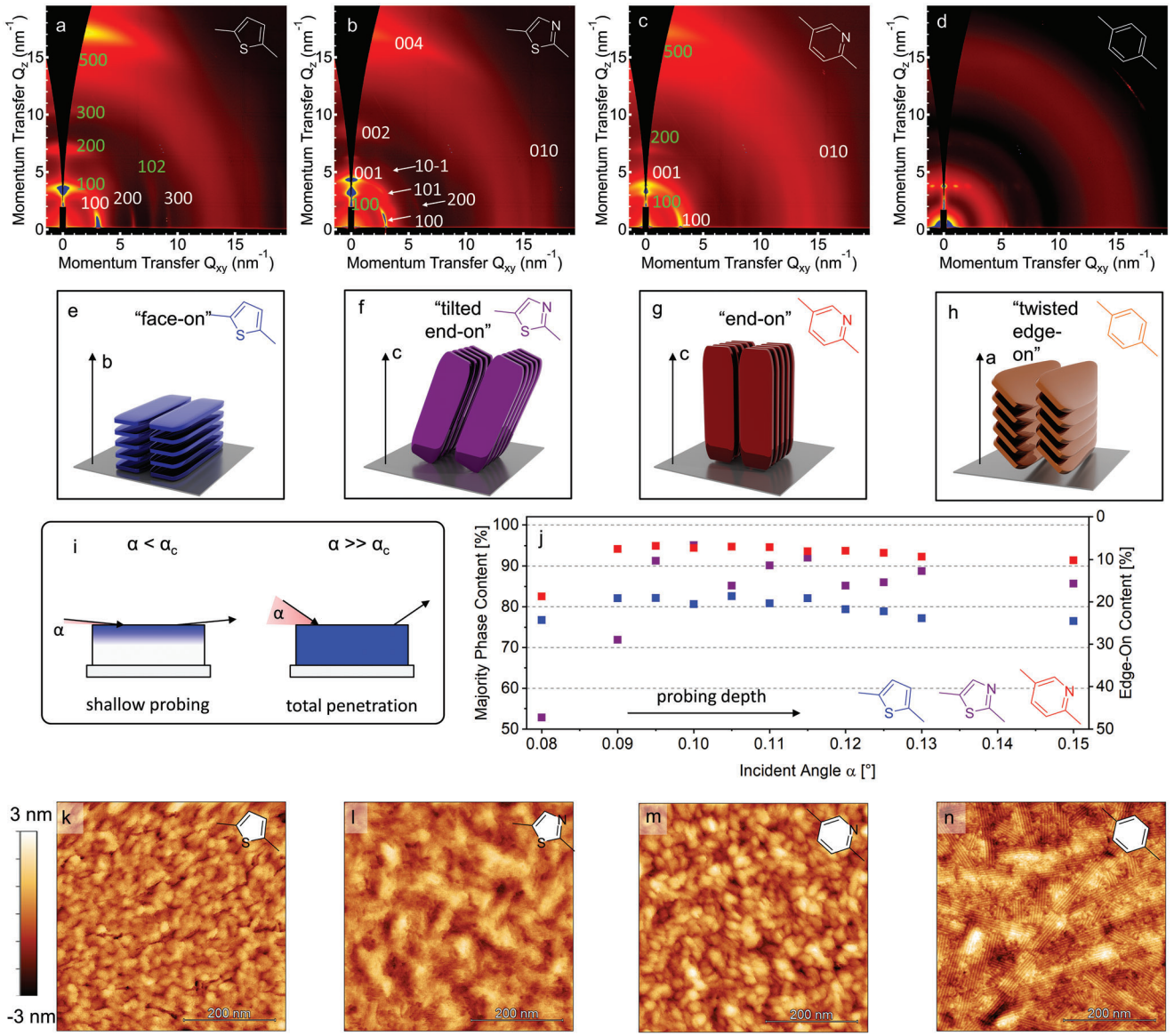


**Figure 3.** a–d) 2D GIWAXS patterns and e–h) sketches of the inferred crystallite textures of high-temperature annealed films (320 °C, 10 min) of the acceptor$_1$–acceptor$_2$ copolymers with different aromatic linkers. Peaks associated with the majority texture/phase are annotated with white, while peaks associated with the minority texture/phase are with green integers. i) Schematics of the penetration and probing depth of GIWAXS dependence on the X-ray incident angle. j) The depth-dependent texture content (majority phase content in %) throughout the polymer films. k–n) AFM height images (500 nm × 500 nm) of high-temperature annealed polymer films (320 °C, 10 min).

scattering patterns of shallow and steep incident angles are compared in Figure S13 (Supporting Information). Therefore, it can be concluded that the textures are not homogeneously distributed throughout the entire film thickness. Instead, a depletion of the majority phase (face-on or end-on) and accumulation of the edge-on minority texture is observable close to the polymer–air interface. Generally, the substrate-polymer interface can favor a different texture than the polymer–air interface, e.g., caused by different surface energies or rarely epitaxial effects.[36,40] In this case, during annealing at elevated temperatures, two competing textures are induced at the two interfaces that consequently occur as gradients in the film after cooling. Therefore, it is likely to assume that the air interface induces a short-range edge-on textured surface layer in the analyzed materials. In the case of the studied samples, the morphology in a major part of the film thickness, however, is decided by the Si substrate, which favors face-on crystallites in the case of P1-[T] and an end-on chain orientation for P2-[Tz] and P3-[Py]. For P4-[Ph], the texture throughout the film is steady, as the anisotropic 100 signals is always exclusively located on the $Q_z$ axis. At a low incident angle of 0.08° in Figure S13d (Supporting Information), a relatively low amorphous signal and a higher number of peaks can be observed than at the critical angle, hinting at increased order at the surface. The likely reason is that both the air-polymer and the substrate-polymer interface favor an edge-on-like texture. However, as the 2D scattering patterns significantly differ from typical conjugated polymer

**Table 2.** Unit cell parameters and textures of the copolymers annealed at 320 °C determined via GIWAXS analysis.

| | P1-[T] | P2-[Tz] | P3-[Py] | P4-[Ph] |
|---|---|---|---|---|
| *a* [Å] | 18.2 | 21.9 | 18.4 | 16.7 |
| *b* [Å] | 3.8 | 3.8 | 4.4 | 12.4 |
| *c* [Å] | 16.1 | 16.1 | 15.4 | 60.3 |
| $\alpha$ [°] | 90 | 90 | 90 | 90 |
| $\beta$ [°] | 90 | 67.5 | 90 | 90 |
| $\gamma$ [°] | 90 | 90 | 90 | 90 |
| Majority texture | Face-on | End-on | End-on | Edge-on-like |
| Minority texture | Edge-On | Edge-on | Edge-on | / |
| Majority texture content [%] at $\alpha_c$ | 78 | 97 | 89 | |
| Lattice | Orthorhombic | Monoclinic | Orthorhombic | Orthorhombic |

patterns, the crystallites and texture likely also differ from the classical edge-on crystallites.

The polymer surface was further investigated with atomic force microscopy (AFM). Intuitively, the topographic order increases during thermal treatment (cf. Figures S14–S17, Supporting Information). Before annealing, all materials exhibit fine-grain anisotropic structures without distinguishable crystalline features. After heating the polymers to 200 °C for 90 minutes, an increase in order is observable, culminating in distinct structures after high-temperature annealing. The respective height images are included in Figure 3k–n. P1-[T] and P3-[Py] form grainy structures, while P2-[Tz] develops fibrillar domains. Conversely, in the polymer P4-[Ph], which exhibits low crystallinity, according to GIWAXS studies, extraordinarily ordered lamellar superstructures cover the entire surface after the low-temperature annealing step. After high-temperature annealing, the respective domains exhibit increased ordering and domain sizes. The lamellar spacing was determined to be ≈60 Å, via Fourier transformation and radial averaging of the AFM image (cf. Figure S18, Supporting Information). This length coincides with the length of the crystallographic *c*-axis of this material, determined via GIWAXS (cf. Table 2). We, therefore, conclude that each lamella of the observed superstructure consists of 2D arrays of P4-[Ph] crystallites.

Complementary NEXAFS analysis of the sulfur and carbon K-edge was employed for the characterization of the polymers by recording total and partial electron yield (TEY and PEY). Generally, NEXAFS spectra are recorded in the energy interval surrounding the element-specific absorption edges, at which excitation of core electrons into the continuum effects a sudden increase of light-matter interaction. Additionally, the absorption edges are overlaid with a fine structure, caused by excitations of core electrons in unpopulated orbitals. Such resonant transitions are sensitive to the bonding environment of the absorbing atom. Additionally, synchrotron sources allow the study of the polarization dependence of directional bonds and hence molecular orientations using linearly polarized X-rays. In contrast to GIWAXS, this method is selectively sensitive to the uppermost polymer layers, and not the entirety of the film thickness under consideration of the PEY and TEY.[41] Compared to carbon K-edge NEXAFS spectra, sulfur-selective K-edge measurements have the advantage of less convoluted spectra due to the less number of different sulfur species in the polymer. During measurement, incident X-rays resonate with the anisotropic transition dipoles of the sulfur species. The strength of this resonance is dependent on the angle between the X-ray beam and these dipoles. In turn, the average surface-relative orientation of the polymer chains can be determined.[42]

Multi K-edge NEXAFS spectra were recorded for different elements under variation of the incident beam-substrate angle ($\theta$ = 20°, 40°, 55°, 70, and 90° for carbon, nitrogen, and oxygen, $\theta$ = 20 °, 55°, and 90° for sulfur), as depicted in **Figure 4**. The step-edge is convoluted with a multitude of peaks that correspond to different directional excitations of core electrons to excited states.[43] Simulations of the transitions of the common sulfur-containing TPD motif of all polymers, were performed via first-principle DFT calculations, as shown in Figure S19a,b (Supporting Information). When the directionality of the transitions relative to the surface normal is determined from the NEXAFS measurements, the orientation of the polymer chain can be deduced, as depicted in Figure 4i. For this interpretation, a planar and linear backbone is assumed. The NEXAFS spectra, recorded for all four element edges, exhibit pronounced dichroism under variation of the incident angle. The total electron yield (TEY) spectra for the carbon and sulfur K-edge are included in Figure 4a–d,e–h). Supplementary carbon, oxygen, and nitrogen K-edge measurements, including total and partial electron yield, can be found in Figures S20–S22 (Supporting Information). From the dichroism, the average angle of each transition vector can be determined according to Equation (1).[42]

$$I = \frac{1}{3}\left[1 + \frac{1}{2}\left(3\cos^2\theta - 1\right)\left(3\cos^2\langle\alpha\rangle - 1\right)\right] \quad (1)$$

The pre-edge transition in the carbon spectra corresponds to the C 1s → $\pi^*$ transition and is therefore oriented normal to the plane of the $\pi$-conjugated system, or along $\alpha_b$ in Figure 4i. The angles $\alpha_a$ and $\alpha_c$ are not easily accessible in carbon K-edge data due to peak convolution with additional core-excited transitions and the step-edge. Complementarily, the angle between the substrate normal and the polymer backbone $\alpha_c$ is accessible under consideration of DFT-based peak assignment (Figure S19, Supporting Information) via sulfur K-edge NEXAFS measurements. The transition peak shows high dichroism and is situated at lower energies than the step edge.

The fit curves and the average angle of the respective transition are depicted in Figure 4j for carbon K-edge and Figure 4k for sulfur K-edge data. A large angle $\alpha_b$ between the C → $\pi^*$-transition and the substrate normal is apparent, indicating a tilted edge-on or end-on type polymer texture on the polymer–air interface. Under consideration of the large angle $\alpha_c$ between the surface-normal and the polymer backbone, a possible end-on texture can be ruled out, proving a superficial edge-on orientation of the polymer chains. This observation agrees with the previous GIWAXS-based observation of the accumulation of oriented chains on the polymer–air interface that does not exhibit an end-on orientation (cf. Figure 3i–j). The angle $\alpha_a$, not directly accessible via the available NEXAFS data, can be calculated based on the orthogonality of the three averaged angles $\alpha_a$, $\alpha_b$, and $\alpha_c$, which are compiled in Table S1 (Supporting Information).

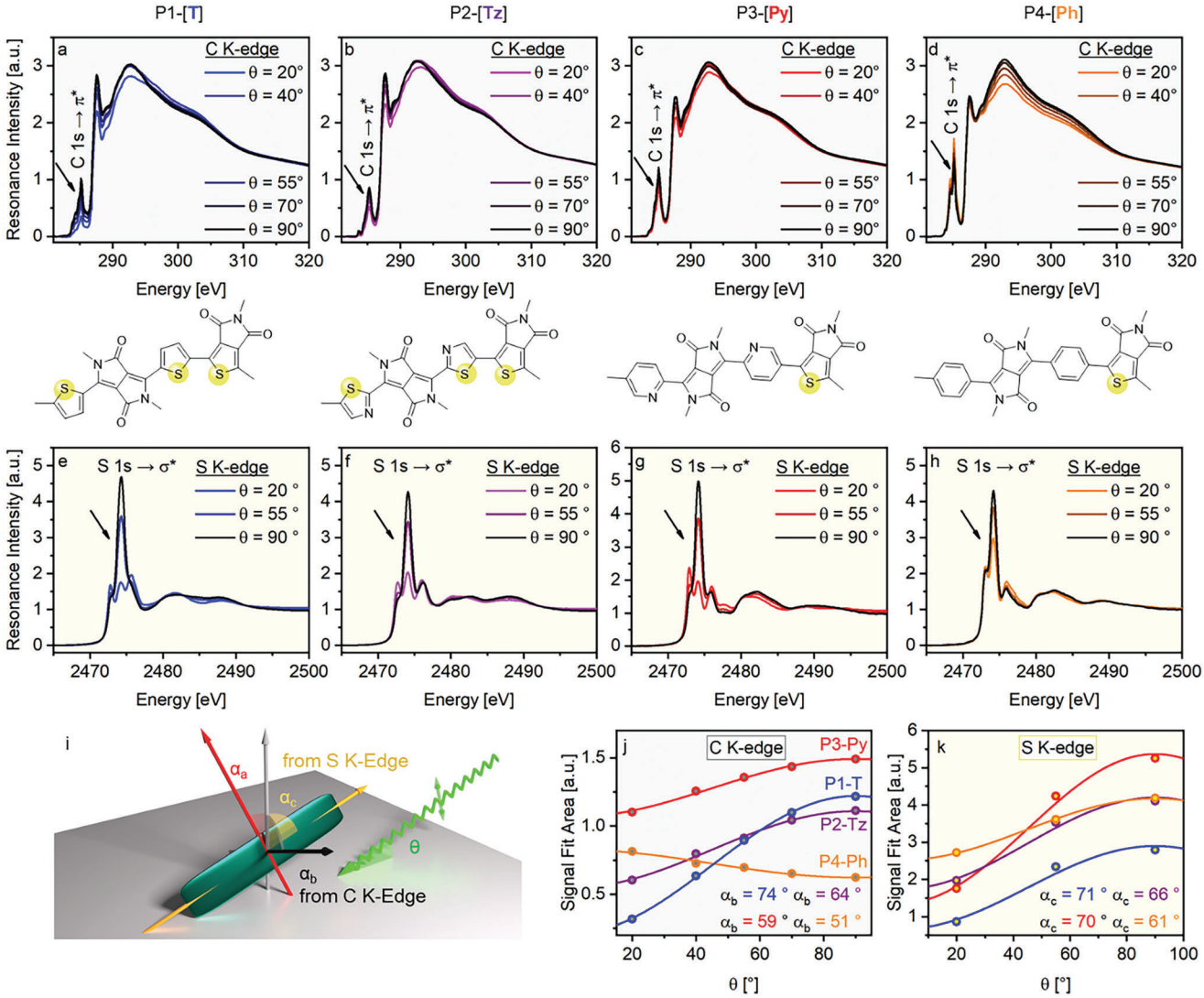


**Figure 4.** a–d): Experimental carbon K-edge NEXAFS spectra of the investigated polymers under five different incident angles, $\theta = 20$, 40, 55, 70, and 90 degrees. e–h) Experimental sulfur K-edge NEXAFS spectra of the investigated polymers under three different incident angles, 20, 55, and 90 degrees. i) Scheme showing the relationship between the angles $\alpha$ and the substrate-relative polymer orientation. j) Fit area of the carbon C 1s → $\pi$* transition at 285 eV with fitted angles $\alpha_b$ between the substrate-normal and the respective transition. k) Fit values of the sulfur S 1s → $\sigma$* transition at 2474 eV and average angles $\alpha_c$ between the substrate-normal and the polymer backbone.

The low dichroism of P4-[Ph] stands out, either due to a lower tilt of the polymer chains, the relatively high amorphous content, or an interchain rotation. Disordered chains contribute randomly oriented vectors to the average value, leading to an approach of the fit values to the magic angle of 54.7°.[42] Considering the highly ordered nature of the material surface determined via AFM, the calculated angles likely reflect the actual chain orientation or are caused by a periodically twisted polymer backbone. In oxygen and nitrogen K-edge NEXAFS, the low-energy features correspond to excitations orthogonal to the $\pi$-conjugated system as in C K-edge data. The dichroism qualitatively matches the previously determined chain orientation. If total electron yield (TEY) and partial electron yield (PEY) are compared, an increased dichroism can be seen in the slightly more surface-sensitive PEY data. This indicates a thin layer of edge-on oriented crystallites on the polymer–air interface.

The polymer pairs P1-[T]/P2-[Tz] and P3-[Py]/P4-[Ph] differ by substituting a carbon via one nitrogen heteroatom in the flanking unit of the DPP moiety in the polymer main chain. This is reflected by the NEXAFS data, as additional low-energy transitions are found for P2-[Tz] and P4-[Ph] when compared to the respective counterparts. We infer that these transitions are caused by N 1s → $\pi$* excitation from thiazolyl- and pyridyl nitrogen core electrons. Therefore, the average dihedral angle between the DPP and TPD units, relative to the respective aromatic linker, can be determined for P2-[Tz] and P3-[Py]. As shown in Figure S21 (Supporting Information), the angle $\alpha_b$ of the N 1s → $\pi$* transition between the aromatic linkers and imide transitions are identical internally for both polymers. This either is an indication for

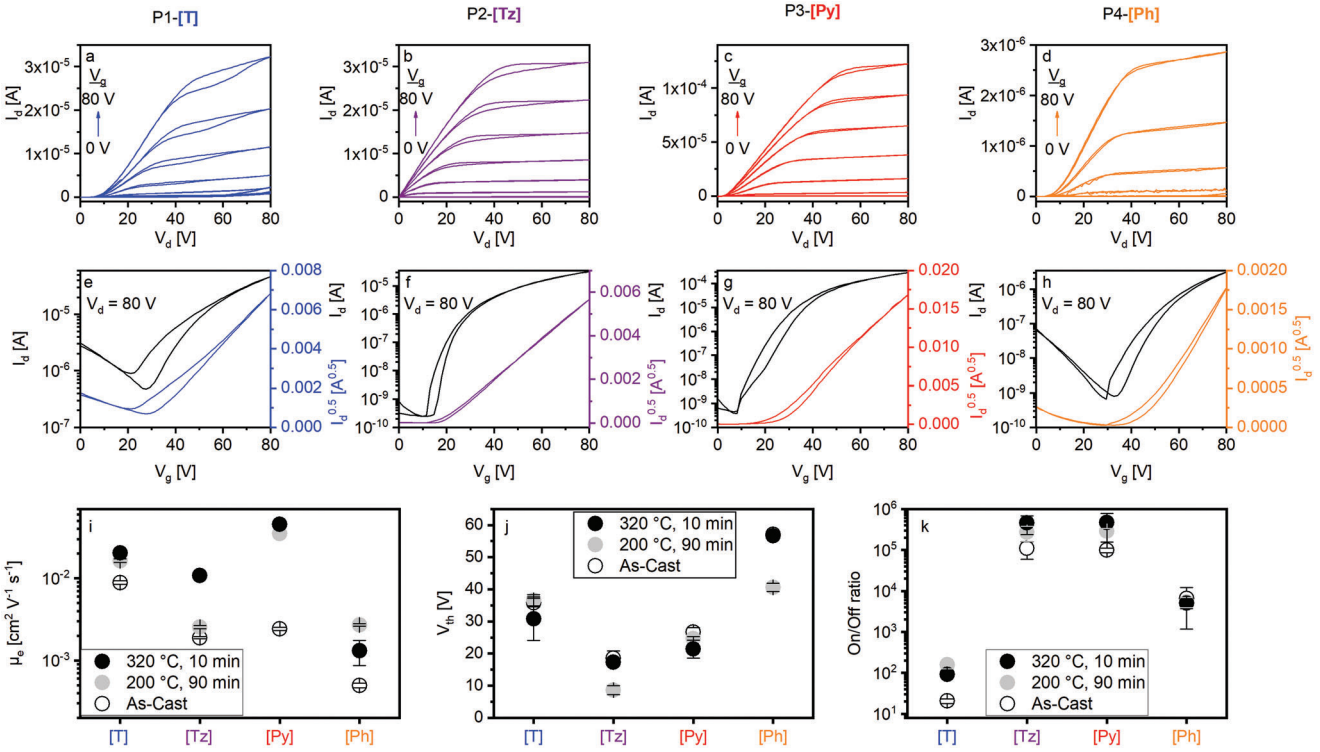


**Figure 5.** a–d) Output and e–h) transfer curves of OFETs for acceptor$_1$–acceptor$_2$ copolymers, P1-[T], P2-[Tz], P3-[Py], and P4-[Ph] after high-temperature annealing (10 min at 320 °C, cooling with 1 K min$^{-1}$) for top gate – bottom contact devices with a channel length of 20 µm. The determined benchmark values are plotted in (i–k).

backbone dihedral angles close to 0° or an internal compensation, e.g., by opposite and equally pronounced rotation of the aryl flanking units in DPP.

### 2.4. Charge Transport

The charge transport properties of the polymers were investigated using top-gate/bottom-contact organic field effect transistor (OFET) devices. The employed architecture, consisting of gold source and drain electrodes, a CYTOP dielectric, and a silver gate electrode, has proven to be reliable for the determination of electron transport properties.[44,45] Optionally, the gold electrodes can be modified with an ultrathin ethoxylated poly(ethylenimine) (PEIE) layer to alter the work function and ease charge injection. However, due to the relatively low thermal stability of this interlayer, it is not feasible for studies including high-temperature annealing steps. To obtain transport properties under comparable conditions, we, therefore, do not include such an interlayer in any device. Instead, the polymer is spin-cast directly on the patterned gold electrode and thermally treated under inert conditions.

The annealing protocol is matched to the conditions used for GIWAXS, NEXAFS, and AFM studies. All polymers are characterized as cast, annealed at 200 °C for 90 min and close to the melting point at 320 °C for 10 min, followed by controlled slow cooling at 1 K min$^{-1}$.

Output characteristics in **Figure** 5a–d demonstrate pronounced acceptor behavior for all polymers after high-temperature annealing for 10 min at 320 °C and slow cooling (1 K min$^{-1}$). Under consideration of the transistor characteristics of the untreated materials and the films annealed at 200 °C for 90 min in Figures S23–S25 (Supporting Information), an increase in current and decrease of hysteresis is observable for devices annealed at 320 °C at 10 min. OFETs having P1-[T] and P4-[Ph] show conductivity at low gate voltage and high drain potential, which is indicative of hole transport contribution to the current flow. This ambipolarity was confirmed in Figure S24 (Supporting Information), where donor output curves could be recorded for those two materials. In contrast, P2-[Tz] and P3-[Py] show no hole transport under the tested conditions, probably due to the increased electron deficiency of the thiazolyl and pyridyl units. Transfer characteristics, depicted in Figure 5e–h and Figure S25 (Supporting Information), show near-ideal behavior for the thiazolyl-linked polymer, with a linear current increase of $\sqrt{I_{SD}}$ with low hysteresis.

The charge carrier mobility $\mu_{sat}$ was extracted from the transfer curves in the saturation regime, according to Equation (2) with the OFET channel length and width $L$ and $W$, the areal capacitance $C_i$ of the CYTOP dielectric, the source-drain current $I_{SD}$, and gate-source potential $V_{GS}$.[46]

$$\mu_{sat} = \frac{2L}{WC_i} \cdot \left( \frac{\partial \sqrt{I_{DS}}}{\partial V_{GS}} \right)^2 \quad (2)$$

To avoid mobility overestimation, transfer curves were linearly fitted at gate voltages above 55 V.[47] The extracted values

**Table 3.** Average OFET values of the series of acceptor$_1$–acceptor$_2$ copolymers, extracted from the transfer characteristics of at least four top gate-bottom contact devices after different thermal treatment protocols.

| | $\mu_e$ [cm$^2$ V$^{-1}$ s$^{-1}$] | $V_{th}$ [V] | $I_{On}/I_{Off}$ | $\mu_e$ [cm$^2$ V$^{-1}$ s$^{-1}$] | $V_{th}$ [V] | $I_{On}/I_{Off}$ | $\mu_e$ [cm$^2$ V$^{-1}$ s$^{-1}$] | $V_{th}$ [V] | $I_{On}/I_{Off}$ |
|---|---|---|---|---|---|---|---|---|---|
| | As-cast | | | 90 min, 200 °C | | | 10 min, 320 °C, 1 K min$^{-1}$ | | |
| P1-[T] | $8.9 \times 10^{-3}$ | 35.9 | $2 \times 10^1$ | $1.6 \times 10^{-2}$ | 36.6 | $2 \times 10^2$ | $9.0 \times 10^{-3}$ | 30.8 | $1 \times 10^2$ |
| P2-[Tz] | $1.9 \times 10^{-3}$ | 18.5 | $1 \times 10^5$ | $2.6 \times 10^{-3}$ | 8.61 | $3 \times 10^5$ | $1.1 \times 10^{-2}$ | 17.3 | $5 \times 10^5$ |
| P3-[Py] | $2.4 \times 10^{-3}$ | 26.7 | $1 \times 10^5$ | $3.5 \times 10^{-2}$ | 24.7 | $3 \times 10^5$ | $4.6 \times 10^{-2}$ | 21.4 | $5 \times 10^5$ |
| P4-[Ph] | $5.0 \times 10^{-3}$ | 57.1 | $7 \times 10^3$ | $2.7 \times 10^{-3}$ | 40.6 | $5 \times 10^3$ | $1.3 \times 10^{-3}$ | 56.7 | $5 \times 10^3$ |

compiled in Figure 5i and **Table 3** demonstrate the beneficial effect of thermal treatment on the charge carrier mobility for all materials. This can be correlated to the increased ordering, as observed in GIWAXS and AFM studies. Improved crystallinity enhances the charge transport properties of conjugated polymers. Additionally, the superficial layer of edge-on crystallites, observed in both angle-resolved GIWAXS and NEXAFS analysis, might further support effective lateral charge transport along the polymer /dielectric interface. P1-[T] reaches a relatively high electron mobility of $\mu_e = 2.0 \times 10^{-2}$ cm$^2$ V$^{-1}$ s$^{-1}$ and moderate hole mobility of $\mu_h = 3.1 \times 10^{-3}$ cm$^2$ V$^{-1}$ s$^{-1}$ after high-temperature annealing. In contrast, P2-[Tz] is an unipolar acceptor material with electron mobility of $\mu_e = 1.1 \times 10^{-2}$ cm$^2$ V$^{-1}$ s$^{-1}$ after the same treatment. The highest mobility of $\mu_e = 4.6 \times 10^{-2}$ cm$^2$ V$^{-1}$ s$^{-1}$ is reached in P3-[Py], the polymer with the highest electron affinity in the series. In P4-[Ph], a low electron mobility of $\mu_e = 1.3 \times 10^{-3}$ cm$^2$ V$^{-1}$ s$^{-1}$ was recorded. This low value can be explained by high internal dihedral angles between the phenyl and DPP units, resulting in a low orbital overlap despite the apparent highly ordered supramolecular structures formed. Upon thermal treatment, the threshold voltage of the polymers shifts marginally from as cast to those annealed at 320 °C, as given in Table 3 and depicted in Figure 5j. However, both the increase and decrease of the threshold voltages can be observed without obvious correlation. Further, chemical structures of the polymers play a decisive role as discussed below. The electron-rich thienyl-linked, and the phenyl-linked polymers lead to transistors with high threshold voltages, while the thiazolyl- and pyridyl-linked polymers result in lower threshold values. The trend, however, is not solely determined by the electron affinity, as the polymer with the higher EA, P3-[Py], exhibits slightly higher threshold voltages than P2-[Tz]. This might be caused by the weak non-ideality observed in the transfer characteristics for the pyridine-linked polymer or variations in the polymer topology.[48] The absence of hole conduction in P2-[Tz] and P3-[Py] results in remarkable on/off current ratios of $5 \times 10^5$ for both polymers. The influence of electron-rich thiophene linkers resulting in ambipolar behavior is reflected in the polymer P1-[T] where low on/off current ratios of $10^1$–$10^2$ were obtained for as-cast as well as annealed samples. For the ambipolar devices, the respective hole mobilities, their threshold voltages, and on/off ratios are included in Figure S26 and Table S2 (Supporting Information). For hole transport, P1-[T] exhibits a lower threshold voltage then P4-[Ph], which is in accordance to the higher IP of P1-[T], compared to P4-[Ph].

Potential overall improvements in the electrical transport properties may be achievable by optimized device architecture (low work function electrodes like Ca or thiol functionalized Au for electron transport), altered dielectric like divinyltetramethyldisiloxane-bis(benzocyclobutene) (BCB).[49] Further, improvements are also possible by optimizing processing parameters (eg. solvent vapor annealing, additives etc.) which can influence the alignment.

### 2.5. All-Polymer Solar Cells

In high-performance organic photovoltaic (OPV) systems reported in the literature, donor–acceptor copolymers are employed as donor components along with fullerene or non-fullerene acceptors in a bulk heterojunction blend layer. Acceptor$_1$–acceptor$_2$ copolymers, like those investigated here, are not commonly used in a polymer-polymer blend. However, the high electron mobility, unipolarity, and low energy absorption of some of the materials hint at a possibility to realize all-polymer blend OPV devices. To investigate this hypothesis, inverted all-polymer OPV devices were prepared with the polymer PBDB-T-2F (PM6) (**Figure 6a**) as the donor component. The frontier orbital energies of PM6 and the different acceptor copolymers are compiled in Figure 6b.[50]

In Figure 6c, the JV curves of the devices employing the four different copolymers as acceptor components are depicted with the average power conversion efficiency (PCE) denoted. The two ambipolar copolymers P1-[T] and P4-[Ph] display very poor performance in all aspects despite the respectable OFET electron mobility. Based on the relative ionization potentials of PM6 and P1-[T], we assume that the energy levels did not allow for the efficient harvesting of the charges generated on the acceptor polymer P1-[T] in this system. This is supported by the neglectable EQE at the absorption wavelengths of P1-[T], indicating that the charges from the excited state of the donor are not efficiently extracted. Therefore, the respective EQE curve in Figure 6e, mostly resembles the absorption of PM6. For the P4-[Ph]-containing system, a low optical density (*cf.* Figure S27, Supporting Information) and the absence of crystallinity (cf. Figure S11, Supporting Information) in the as-cast state are likely to be detrimental to the device performance.

Devices with the two unipolar acceptors P2-[Tz] and P3-[Py], in contrast, lead to comparably higher $J_{SC}$, $V_{OC,}$ and PCE. Between these two materials, the pyridyl-linked copolymer/PM6 system shows a higher $J_{SC}$ compared to P2-[Tz]/PM6 system. While a correlation between the $J_{SC}$ and charge carrier mobility is likely and follows the trend observed in OFET measurements, reliable correlation requires quantification of the bulk transport, e.g. based on space charge limited current (SCLC), charge extraction by

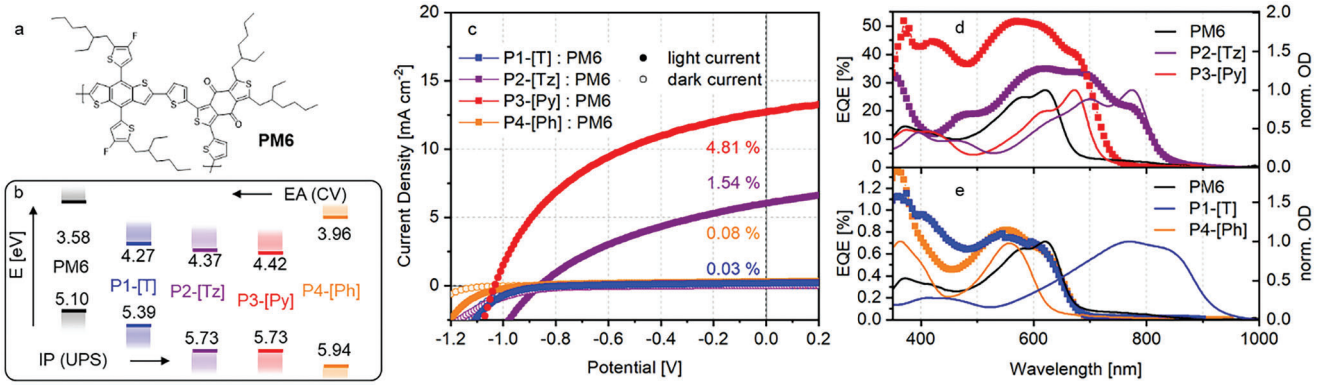


**Figure 6.** a) Chemical structure of donor polymer PM6, b) ionization energies donor and acceptor frontier orbital levels, c) light and dark JV curves, and d) EQE data for all-polymer solar cells employing P2-[Tz]: PM6 and P3-[Py]: PM6 blends as active layers overlaid with the thin film UV–vis absorption of the respective components. e) EQE data for all-polymer solar cells employing P1-[T]: PM6 and P4-[Ph]: PM6 blends as active layers overlaid with the thin film UV–vis absorption of the respective components.

linearly increasing voltage (CELIV) or time of flight (ToF) characterization. Remarkably, a high $V_{OC}$ above 1 V is reached for this polymer blend. However, the low fill factors with a maximum of 44% strongly restrict the PCE of the devices indicating more space for improvement of the device performance by decreasing the series resistance and increasing the parallel resistance.

To investigate the influence of morphology and structure of the active layers on device performance, further AFM and GIWAXS thin film analysis was conducted on films, which were coated and treated under conditions representative for the OPV. AFM height and phase images (Figures S28 and S29, Supporting Information) did not reveal any obvious variation in domain size and phase separation, suggesting that differences in performance metrics did not stem from changes of the internal donor–acceptor interface area. In contrast, GIWAXS of blend films did reveal variations in absolute scattering strength and relative intensity of the 010 ($\pi$–$\pi$ stacking) signal between the different active layer blends (Figure S30, Supporting Information). Strikingly, the polymer blend containing P4-[Ph] is significantly less ordered than the remaining mixtures.

Overall, we assume that optimization of the blend composition, crystallinity, and morphology, e.g., via additivation or annealing, can lead to improved performance. Yet, the best copolymer in the series of acceptor$_1$–acceptor$_2$ copolymers leads to devices with an average PCE of 4.8%, based on six devices (Best device: 5.2%). In comparison, BHJ devices using PM6 as donor in combination with the donor–acceptor copolymer N2200 consisting of alternating naphthalenediimide and bithiophene units as acceptor were reported to achieve 8.3% PCE.[51] If a polymerized derivative of the non-fullerene acceptor Y6 (BTP-4F) is employed instead of N2200, a PCE of 15.2% was reached in binary polymer blends.[52]

## 3. Conclusion

Motivated by the need for new design principles for acceptor polymers, a series of four acceptor$_1$–acceptor$_2$ copolymers, based on the classical building blocks diketopyrrolopyrrole (DPP) and thienopyrrolodione (TPD) was synthesized using direct aryl polymerization and thoroughly investigated with respect to structure-function relationships in thin film devices. The difference between the polymer structures was the nature of the aryl flanking unit of the DPP core. By variation from a thienyl- to a thiazolyl-, pyridyl, and phenyl linker, substantial differences in a multitude of optoelectronic and structural properties were apparent. Optoelectronic properties, like the optical gap, ionization potential, and electron affinity, roughly followed the electron deficiency of the flanking unit. The one exception was the sterically demanding phenyl linker, which introduces a large dihedral angle to the polymer backbone, leading to disturbed $\pi$-conjugation. Overall, all materials in the series exhibit extremely high electron affinities, which are reported to be beneficial for operational stability. Structural investigations, based on grazing incidence wide-angle x-ray scattering (GIWAXS), reveal vastly different film morphologies, varying between face-on or end-on textured crystallites and lamellar superstructures after thermal treatment. In accordance with atomic force microscopy (AFM) and NEXAFS studies, a superficial layer of edge-on oriented chains was shown for all materials. Additionally, NEXAFS studies indicate a tilted edge-on or end-on type polymer texture on the polymer–air interface and almost negligible dihedral angles in P2-[Tz] and P3-[Py]. Holistically, these differences are reflected when these polymers are applied in field-effect transistors and all-polymer solar cells. Electron mobilities of a maximum of $4.6 \times 10^{-2}$ cm$^2$ V$^{-1}$ s$^{-1}$ were determined after high-temperature annealing with outstanding on/off current ratios of $8 \times 10^5$ for the highly electron-deficient pyridyl-linked copolymer P3-[Py]. In contrast, the polymers linked with more electron-rich (or less electron-deficient) units, P1-[T] and P4-[Ph] exhibited ambipolar behavior in OFETs with orders of magnitude lower charge carrier mobility and low $I_{on}/I_{off}$ ratios. An average PCE of 4.8% with an open circuit voltage above 1 V was measured for all-polymer blend solar cells with the pyridyl-linked copolymer P3-[Py] in combination with PM6 as donor; being the best among the tested polymers.

## 4. Experimental Section

*Materials*: Reactions sensitive toward humidity and oxygen were conducted under a protective argon atmosphere in Schlenk apparatuses, which were previously flame-dried under high-vacuum. Anhydrous

solvents were purchased from Sigma-Aldrich / Acros Organics in sealed bottles with molecular sieves and used as received. All other solvents, for example, for workups or Soxhlet extractions, were freshly distilled in-house.

$CDCl_3$ (99.95%) was supplied by Deutero, Germany. Cesium carbonate (≥ 99%), and potassium carbonate (99.5%) were purchased from Sigma-Aldrich and dried at 500 °C under high vacuum before synthesis. Reagents were used as received from commercial sources, if not stated differently. CYTOP-809 was purchased from AGC Chemicals Co. and used as received without dilution. Reactions under microwave irradiation were carried out using a Biotage Initiator+ synthesis microwave. NMR spectra were recorded on a Bruker Avance spectrometer (300 MHz) at room temperature.

*Ultraviolet Photoelectron Spectroscopy (UPS)*: UPS measurements were carried out on a PHI 5000 VersaProbe III system fitted with a He discharge light source providing stable and continuous He I and He II lines under ultrahigh vacuum (ca. $10^{-9}$ mbar). Samples for UPS measurements were obtained by spin-coating doped poly(DPP-TPD) solutions on clean ITO (15 Ω $sq^{-1}$), affording ca. 20 nm thick films (measured by using a dummy sample in a profilometer). The samples were transferred from the evaporation chamber to a $N_2$-filled glove box and further to the instrument in a nitrogen-filled and sealed stainless steel transport vessel. Once the samples were loaded into the instrument main chamber, He I source (50 W) was used to induce photoelectrons and were collected at a 90° take-off angle by using a multichannel semi-spherical analyzer. Both valence band maximum (VBM) and secondary electron cutoff (SECO) signals from the samples were measured by applying −5 V between the analyzer and the substrate. Both VBM and SECO spectra were collected in at least three different areas in two different samples, and only the reproducible measurements were considered for further calculations and discussion. The VBM and SECO binding energy values necessary to determine ionization potential and work function, respectively, were obtained by the linear extrapolation method. The Fermi level $E_F$ of the samples was referenced to the Fermi level of sputter-cleaned Au foil. The energy resolution of the VBM and SECO is 0.15 eV, which was derived from the full-width half-maximum of the Au Fermi edge.

*Atomic Force Microscopy (AFM)*: The surface morphologies of neat semiconductor films were imaged using a Bruker Dimension Icon AFM at the Melbourne Center for Nanofabrication (MCN). AFM measurements were operated in the ScanAsyst mode. AFM measurements of blend films were carried out using a Nanosurf Easyscan 2 FlexAFM in tapping mode with different magnifications. The data were processed using Gwyddion.

*Near Edge X-Ray Absorption Fine Structure (NEXAFS) Spectroscopy*: Carbon, Nitrogen, and Oxygen K-edge NEXAFS measurements were performed at the soft X-ray spectroscopy beamline at the Australian Synchrotron.[53] All samples were spin-cast on pre-cleaned silicon substrates and subjected to high-temperature annealing at 320 °C for 10 min in a $N_2$ glovebox, followed by controlled cooling with a rate of 1 K $min^{-1}$. Angle-resolved NEXAFS spectra ($\theta = 90°$, 70°, 55°, 40°, and 20°) at different K-edges were measured under high vacuum to find the tilt angle of the polymer backbone. Data were analyzed with the assistance of the QANT software.[54]

Sulfur K-edge NEXAFS experiments were performed at the MEX2 beamline at the Australian Synchrotron. Total electron yield (TEY) mode was employed, where X-ray absorption was measured via recording the drain current flowing to the sample to replenish electrons lost due to photoemission. Samples were prepared on bare, highly doped silicon wafers and measured under high vacuum. Angle-resolved NEXAFS spectra ($\theta = 90°$, 55°, and 20°) at different K-edges were measured to find the tilt angle of the polymer backbone.

*OFET Device Characterization and Fabrication*: Bottom contact/top gate organic field effect transistors were prepared on patterned FET substrates fabricated in the Melbourne Centre of Nanofabrication (MCN). Each substrate consisted of 16 devices with a constant channel width $W$ of 10 mm and varying channel lengths $L$ of 2.5–20 µm. The source and drain electrodes were a 30 nm thick gold layer on a 10 nm chrome adhesion layer. The devices were prepared by cleaning in acetone and subsequently in isopropanol in an ultrasonic bath for 15 min, followed by 15 min plasma treatment. Thin polymer films were spun cast from 10 mg·$mL^{-1}$ $CHCl_3$ solutions at a spinning speed of 3000 rpm under ambient conditions, followed by deposition of a 500 nm CYTOP layer (relative permittivity k ≈ 2.1, $C_i = 3.7$ nF/$cm^2$) by spin casting at 9000 rpm for 2 min on the active polymer layer in a nitrogen glovebox. Residual solvents were removed by heat treatment at 110 °C for 1 h. A 50 nm Al gate electrode was thermally deposited under high vacuum at a constant rate of 1 Å $s^{-1}$.

Using Equation (2), the charge carrier mobility $\mu$ was calculated from the slope of the $(I_D)^{0.5}$–$V_G$ plots, where $V_t$ is the threshold voltage and $C_i$ is the CYTOP dielectric capacitance.

$$I_D = \frac{W}{2L} C_i \mu (V_G - V_t)^2 \quad (3)$$

*Grazing-Incidence Wide-Angle X-Ray Scattering (GIWAXS)*: GIWAXS on neat films coated on silicon substrates was performed in vacuum at RT on the SAXS/WAXS beamline with a photon energy of 15 keV.[55] The setup included a Pilatus 2M detector, which was used to record 2D scattering patterns. Each image consists of three superimposed acquisitions with different relative sample-detector positions at identical distances to obtain gapless scattering data. A silver behenate reference standard was used to calibrate the sample-to-detector distance. The sample and detector were placed in a vacuum chamber to reduce air scatter. The measurements were taken as a function of the angle of incidence, with data shown at an angle of incidence near the critical angle that maximized scattering intensity from the sample. Data evaluation and wedge correction were conducted using a modified Nika software package in IgorPro 8.38.[1] Q-profiles are cake cuts covering an azimuthal angle of 75°–105° for the cuts in the vertical direction and 0°–15° as well as 165°–180° for the cuts in the horizontal direction. Annealed samples were subjected to thermal treatment under nitrogen atmosphere.

Grazing-incidence small-angle x-ray scattering (GIWAXS) of polymer blend films was carried out on a Xeuss 3.0 (Xenocs SAS, Grenoble, France) with a Cu K$\alpha$ source ($\lambda = 1.54$ Å). The scattering patterns were recorded with a Dectris EIGER 2R 1M detector, with 1028 × 1062 pixels and a pixel size of 75 µm × 75 µm, and a sample-to-detector distance of 72 mm. The beam size was adjusted to 0.5 mm × 0.5 mm and each sample was measured for 5 h. The presented q-line cuts are cake cuts covering an azimuthal angle of 70°–110° for the cuts in the vertical direction and 0°–20° as well as 160°–180° for the cuts in the horizontal direction.

*DFT Calculations*: To investigate the relaxed atomic structure of P1, P2, P3, and P4 polymers, the study employed first principles density functional theory calculations as implemented in the Vienna Ab initio Simulation Package (VASP) package.[56–58] In all cases, periodic polymer supercells were constructed with at least three monomers. In the supercell models, bulky side chains were replaced methyl groups to ensure computational feasibility. The study used the generalized gradient approximation (GGA) of the Perdew, Burke, and Ernzerhof (PBE) form for the exchange-correlation functional while ensuring computational accuracy with an energy cut-off of 400 eV.[59–62] Full relaxation of the polymer structures was carried out until the Hellman–Feynman atomic forces were <0.02 eV $Å^{-1}$. The convergence threshold of energy was set at $10^{-4}$ eV. The Brillouin zone was represented using the gamma-centered 3×1×1 k-point grid. Software package VESTA was used to visualize the atomic structures.

*All-Polymer Solar Cell (All-PSC) Device Fabrication*: All-PSCs were fabricated with an inverted device geometry with a structure of ITO/ZnO/active layer/$MoO_3$/Ag. Pre-patterned ITO glass slides were cleaned via ultrasonication in acetone and isopropanol consecutively for 15 min, followed by oxygen plasma treatment for another 15 min. After that, the ZnO (0.1 M) precursor was spin-cast onto the cleaned ITO glass substrates at 3000 rpm for 30 s and then annealed at 200 °C for 30 min under ambient conditions. The active layer solutions were prepared by dissolving PM6 and polymer acceptors at 80 °C in toluene (15 g $L^{-1}$) in a nitrogen glovebox overnight without stirring. No processing additive was used. Immediately before coating, the active layer solutions were mixed in a 1: 1 ratio and spin-cast on top of the ZnO-modified substrates in a nitrogen glovebox. The final film thickness of the cells processed was 90–100 nm. Then, $MoO_3$ (12 nm, 0.2 Å $s^{-1}$) and Ag (100 nm, 0.5 $Å^{-1}$) were thermally deposited on

the active layer under high vacuum ($2 \times 10^{-7}$–$1 \times 10^{-6}$ mbar). The device area was defined as 4.5 $mm^2$ via a shadow mask. All devices were encapsulated with glass cover slides using epoxy resin before testing the device performance in air.

*$^1$H-NMR Spectroscopy*: $^1$H NMR spectra (with 64 – 2048 scans) were recorded using a Bruker Avance 250 spectrometer at a working frequency of 300 MHz. Chemical shifts are given in ppm and coupling constants (J) in Hertz (Hz). The spectra were referenced to the residual solvent peak of $CDCl_3$ ($\delta = 7.26$ ppm).

*Thermogravimetric Analysis (TGA)*: TGA thermograms were recorded using a Mettler Toledo TGA/DSC 3+. Measurements were conducted under $N_2$ atmosphere between 30–700 °C at a heating rate of 10 K $min^{-1}$. Specimens (between 5 and 7 mg) were filled into $Al_2O_3$ crucibles (volume 70 µL).

*Differential Scanning Calorimetry (DSC)*: DSC was recorded using a Perkin Elmer Pyris 1 DSC in the range between 30 and 350 °C with heating and cooling of 10 K $min^{-1}$. The first heating and cooling curves were discarded.

*Differential Scanning Calorimetry (Flash DSC)*: Flash DSC was recorded using a Mettler Toledo flash DSC 1 in the range between 30 and 600 °C with heating and cooling rates ranging from 50 to 1000 K $s^{-1}$. The polymer was placed as a solid crumb on the chip sensor. The first heating and cooling curves used a rate of 2000 K $s^{-1}$ and were used to eliminate the thermal history of the polymer.

*Gel Permeation Chromatography (GPC)*: GPC measurement was performed on an instrument having an SDV linear XL gel column (particle size = 5 µm) with a separation range from 100 to 3 000 000 Da (PSS, Mainz, Germany) together with a refractive index detector (1200 Series, Agilent Technologies). $CHCl_3$ (HPLC grade) was used as the solvent (for dissolving polymer and as eluting solvent) with a flow rate of 0.5 mL $min^{-1}$ at room temperature. As internal standard toluene (HPLC grade) was used. The calibration was done with narrowly distributed polystyrene (PS) homopolymers (PSS calibration kit). An injection volume of 20 µL was used for the measurements. The sample was dissolved in $CHCl_3$ and filtered through a 0.22 µm PTFE filter before analysis.

*Cyclic Voltammetry (CV)*: Cyclic voltammetry was performed using a Gamry Interface 1010 Potentiostat/Galvanostat, working with a three-electrode setup. Polymer films were measured in acetonitrile with $TBAPF_6$ (0.1 M) as electrolyte. Thin films were spin-cast (3000 rpm, 60 s, 40 µL) onto ITO from 10 g $L^{-1}$ solution in $CHCl_3$. The samples were then measured using a Pt-counter-, and a standard $Ag/AgNO_3$ reference electrode for the measurement. All electrolytes were degassed with argon flow for 10 min before each measurement. Scans were recorded at a scan rate of 50 or 100 mV $s^{-1}$, with a step size of 2 mV.

## Supporting Information

Supporting Information is available from the Wiley Online Library or from the author.

## Acknowledgements

A.W.E., J.H., and M.T. acknowledge financial support from Deutsche Forschungsgemeinschaft (DFG) (407706940, TH 807/7-1), the Bavarian State Ministry for Science and Art (SolTech), and the international research training group (IRTG) Optical excitations in organic and inorganic semiconductors (OPTEXC, GRK 2817/1). UPS data were obtained using the PHI 5000 VersaProbe III system in the Keylab Device engineering (BPI). T.T.H. and N.V.M. gratefully acknowledge support from the Australian Research Council (DP220103783) and the computational support from the Australian National Computing Infrastructure and the Pawsey Supercomputing Facility. This research was undertaken on the SAXS/WAXS, Soft X-Ray, and MEX2 beamlines at the Australian Synchrotron, part of ANSTO.[55] The authors acknowledge Wen Liang Tan, Doan Vu (Monash), Nigel Kirby, Chris Glover, and Valerie Mitchell (ANSTO) for assistance during GIWAXS and NEXAFS measurements. This work was performed in part at the Melbourne Centre for Nanofabrication (MCN) in the Victorian Node of the Australian National Fabrication Facility (ANFF). Work at the Molecular Foundry was supported by the Office of Science, Office of Basic Energy Sciences, of the U.S. Department of Energy under Contract No. DE-AC02-05CH11231. The authors thank Rika Schneider for GPC measurements. A.E. thanks Hao Liu and Doan Vu for the introduction to OPV fabrication. This work was also supported by a Senior Research Fellowship (CRM) from the University of Bayreuth Centre of International Excellence "Alexander von Humboldt.".

Open access publishing facilitated by Monash University, as part of the Wiley - Monash University agreement via the Council of Australian University Librarians.

## Conflict of Interest

The authors declare no conflict of interest.

## Data Availability Statement

The data that support the findings of this study are available from the corresponding author upon reasonable request.

## Keywords

$acceptor_1$–$acceptor_2$ copolymers, all-polymer solar cells, microstructure, OFET, organic semiconductors

Received: November 21, 2023
Revised: March 14, 2024
Published online:

[1] H. Shirakawa, E. J. Louis, A. G. MacDiarmid, C. K. Chiang, A. J. Heeger, *J. Chem. Soc. Chem. Commun.* **1977**, *16*, 578.
[2] Q. Gu, A. Abdurahman, R. H. Friend, F. Li, *J. Phys. Chem. Lett.* **2020**, *11*, 5638.
[3] F. Rodella, S. Bagnich, E. Duda, T. Meier, J. Kahle, S. Athanasopoulos, A. Köhler, P. Strohriegl, *Front. Chem.* **2020**, *8*, 657.
[4] S. Holliday, R. S. Ashraf, A. Wadsworth, D. Baran, S. A. Yousaf, C. B. Nielsen, C.-H. Tan, S. D. Dimitrov, Z. Shang, N. Gasparini, M. Alamoudi, F. Laquai, C. J. Brabec, A. Salleo, J. R. Durrant, I. McCulloch, *Nat. Commun.* **2016**, *7*, 11585.
[5] P. Schmode, D. Ohayon, P. M. Reichstein, A. Savva, S. Inal, M. Thelakkat, *Chem. Mater.* **2019**, *31*, 5286.
[6] M. Goel, M. Siegert, G. Krauss, J. Mohanraj, A. Hochgesang, D. C. Heinrich, M. Fried, J. Pflaum, M. Thelakkat, *Adv. Mater.* **2020**, *32*, 2003596.
[7] W. Huang, J. Chen, Y. Yao, D. Zheng, X. Ji, L.-W. Feng, D. Moore, N. R. Glavin, M. Xie, Y. Chen, R. M. Pankow, A. Surendran, Z. Wang, Y. Xia, L. Bai, J. Rivnay, J. Ping, X. Guo, Y. Cheng, T. J. Marks, A. Facchetti, *Nature* **2023**, *613*, 496.
[8] G. Krauss, F. Meichsner, A. Hochgesang, J. Mohanraj, S. Salehi, P. Schmode, M. Thelakkat, *Adv. Funct. Mater.* **2021**, *31*, 2010048.
[9] M. Goel, C. D. Heinrich, G. Krauss, M. Thelakkat, *Macromol. Rapid Commun.* **2019**, *40*, 1800915.
[10] L. Ying, F. Huang, G. C. Bazan, *Nat. Commun.* **2017**, *8*, 14047.
[11] Y. Wang, T. Hasegawa, H. Matsumoto, T. Michinobu, *J. Am. Chem. Soc.* **2019**, *141*, 3566.
[12] Y. Shi, H. Guo, M. Qin, Y. Wang, J. Zhao, H. Sun, H. Wang, Y. Wang, X. Zhou, A. Facchetti, X. Lu, M. Zhou, X. Guo, *Chem. Mater.* **2018**, *30*, 7988.

[13] H. Wu, C. Yang, Q. Li, N. B. Kolhe, X. Strakosas, M. Stoeckel, Z. Wu, W. Jin, M. Savvakis, R. Kroon, D. Tu, H. Y. Woo, M. Berggren, S. A. Jenekhe, S. Fabiano, *Adv. Mater.* **2022**, *34*, 2106235.
[14] J. Wu, S. Yang, S. Wang, Z. Jiang, C. Gao, L. Wang, *Compos. Commun.* **2023**, *37*, 101461.
[15] A. Erhardt, A. Hochgesang, M. Christopher R, M. Thelakkat, *Adv. Electron. Mater.* **2023**, *33*, 2300614.
[16] A. Hochgesang, A. Erhardt, J. Mohanraj, M. Kuhn, E. M. Herzig, S. Olthof, M. Thelakkat, *Adv. Funct. Mater.* **2023**, *33*, 2300614.
[17] C. J. Mueller, C. R. Singh, M. Fried, S. Huettner, M. Thelakkat, *Adv. Funct. Mater.* **2015**, *25*, 2725.
[18] T. Weller, M. Breunig, C. J. Mueller, E. Gann, C. R. McNeill, M. Thelakkat, *J. Mater. Chem. C* **2017**, *5*, 7527.
[19] T. Weller, K. Rundel, G. Krauss, C. R. McNeill, M. Thelakkat, *J. Phys. Chem. C* **2018**, *122*, 7565.
[20] C. J. Mueller, E. Gann, C. R. Singh, M. Thelakkat, C. R. McNeill, *Chem. Mater.* **2016**, *28*, 7088.
[21] B. Carsten, J. M. Szarko, L. Lu, H. J. Son, F. He, Y. Y. Botros, L. X. Chen, L. Yu, *Macromolecules* **2012**, *45*, 6390.
[22] R. M. W. Wolfe, J. R. Reynolds, *Org. Lett.* **2017**, *19*, 996.
[23] J.-R. Pouliot, L. G. Mercier, S. Caron, M. Leclerc, *Macromol. Chem. Phys.* **2013**, *214*, 453.
[24] C. R. Singh, G. Gupta, R. Lohwasser, S. Engmann, J. Balko, M. Thelakkat, T. Thurn-Albrecht, H. Hoppe, *J. Polym. Sci. Part B Polym. Phys.* **2013**, *51*, 943.
[25] P. Josse, P. Chávez, C. Dindault, C. Dalinot, S. M. McAfee, S. Dabos-Seignon, D. Tondelier, G. Welch, P. Blanchard, N. Leclerc, C. Cabanetos, *Dyes Pigments* **2017**, *137*, 576.
[26] K. Kranthiraja, K. Murotani, F. Hamada, A. Saeki, *ACS Appl. Electron. Mater.* **2022**, *4*, 2086.
[27] D. Qu, T. Qi, H. Huang, *J. Energy Chem.* **2021**, *59*, 364.
[28] W. W. Bao, R. Li, Z. C. Dai, J. Tang, X. Shi, J. T. Geng, Z. F. Deng, J. Hua, *Front. Chem.* **2020**, *8*, 679.
[29] X. Yan, K. Fang, H. Liu, C. Xi, *Chem. Commun.* **2013**, *49*, 10650.
[30] C. Scharsich, R. H. Lohwasser, M. Sommer, U. Asawapirom, U. Scherf, M. Thelakkat, D. Neher, A. Köhler, *J. Polym. Sci. Part B Polym. Phys.* **2012**, *50*, 442.
[31] R. Sevinçek, S. Çelik, M. Aygün, S. Alp, Ş. Işık, *Acta Crystallogr. Sect. E Struct. Rep. Online* **2010**, *66*, o1546.
[32] F. C. Spano, *Acc. Chem. Res.* **2010**, *43*, 429.
[33] M. Saito, T. Koganezawa, I. Osaka, *ACS Appl. Polym. Mater.* **2019**, *1*, 1257.
[34] C.-A. Chen, S.-C. Wang, S.-H. Tung, W.-F. Su, *Soft Matter* **2019**, *15*, 9468.
[35] D. Vu, W. L. Tan, L. He, A. Ehm, D. R. T. Zahn, C. R. McNeill, *ACS Macro Lett.* **2023**, *12*, 140.
[36] O. Dolynchuk, P. Schmode, M. Fischer, M. Thelakkat, T. Thurn-Albrecht, *Macromolecules* **2021**, *54*, 5429.
[37] Z. Peng, L. Ye, H. Ade, *Mater. Horiz.* **2022**, *9*, 577.
[38] D. Gao, Z. Chen, Z. Mao, J. Huang, W. Zhang, D. Li, G. Yu, *RSC Adv.* **2016**, *6*, 78008.
[39] J. L. Baker, L. H. Jimison, S. Mannsfeld, S. Volkman, S. Yin, V. Subramanian, A. Salleo, A. P. Alivisatos, M. F. Toney, *Langmuir* **2010**, *26*, 9146.
[40] A.-K. Löhmann, T. Henze, T. Thurn-Albrecht, *Proc. Natl. Acad. Sci* **2014**, *111*, 17368.
[41] O. Dhez, H. Ade, S. G. Urquhart, *J. Electron Spectrosc. Relat. Phenom.* **2003**, *128*, 85.
[42] M. M. Nahid, E. Gann, L. Thomsen, C. R. McNeill, *Eur. Polym. J.* **2016**, *81*, 532.
[43] S. De Kock, K. Skudler, R. Matsidik, M. Sommer, M. Müller, M. Walter, *Phys. Chem. Chem. Phys.* **2023**, *25*, 20395.
[44] P. Kafourou, B. Park, J. Luke, L. Tan, J. Panidi, F. Glöcklhofer, J. Kim, T. D. Anthopoulos, J. Kim, K. Lee, S. Kwon, M. Heeney, *Angew. Chem., Int. Ed.* **2021**, *60*, 5970.
[45] L. Tang, L. Thomsen, C. R. McNeill, *ACS Appl. Polym. Mater.* **2022**, *4*, 5501.
[46] A. Köhler, H. Bässler, *Electronic Processes in Organic Semiconductors: An Introduction*, Wiley-VCH, Weinheim, **2015**.
[47] H. H. Choi, K. Cho, C. D. Frisbie, H. Sirringhaus, V. Podzorov, *Nat. Mater.* **2018**, *17*, 2.
[48] B. Meng, J. Liu, L. Wang, *Nano Mater. Sci.* **2021**, *3*, 113.
[49] H. Phan, M. J. Ford, A. T. Lill, M. Wang, G. C. Bazan, T. Nguyen, *Adv. Funct. Mater.* **2018**, *28*, 1707221.
[50] J. Bertrandie, J. Han, C. S. P. De Castro, E. Yengel, J. Gorenflot, T. Anthopoulos, F. Laquai, A. Sharma, D. Baran, *Adv. Mater.* **2022**, *34*, 2202575.
[51] X. Liu, Y. Zou, H.-Q. Wang, L. Wang, J. Fang, C. Yang, *ACS Appl. Mater. Interfaces* **2018**, *10*, 38302.
[52] H. Yu, S. Luo, R. Sun, I. Angunawela, Z. Qi, Z. Peng, W. Zhou, H. Han, R. Wei, M. Pan, A. M. H. Cheung, D. Zhao, J. Zhang, H. Ade, J. Min, H. Yan, *Adv. Funct. Mater.* **2021**, *31*, 2100791.
[53] B. C. C. Cowie, A. Tadich, L. Thomsen, R. Garrett, I. Gentle, K. Nugent, S. Wilkins, *AIP Conf. Proc.* **2010**, *1234*, 307.
[54] E. Gann, C. R. McNeill, A. Tadich, B. C. C. Cowie, L. Thomsen, *J. Synchrotron Radiat.* **2016**, *23*, 374.
[55] N. M. Kirby, S. T. Mudie, A. M. Hawley, D. J. Cookson, H. D. T. Mertens, N. Cowieson, V. Samardzic-Boban, *J. Appl. Crystallogr.* **2013**, *46*, 1670.
[56] T. D. Huan, R. Ramprasad, *J. Phys. Chem. Lett.* **2020**, *11*, 5823.
[57] A. Alesadi, F. Fatima, W. Xia, D. Kilin, *J. Phys. Chem. B* **2021**, *125*, 8953.
[58] G. Sun, J. Kürti, P. Rajczy, M. Kertesz, J. Hafner, G. Kresse, *J. Mol. Struct. THEOCHEM* **2003**, *624*, 37.
[59] J. P. Perdew, K. Burke, M. Ernzerhof, *Phys. Rev. Lett.* **1996**, *77*, 3865.
[60] Y. Liang, J. Zhao, Y. Yang, S.-F. Hung, J. Li, S. Zhang, Y. Zhao, A. Zhang, C. Wang, D. Appadoo, L. Zhang, Z. Geng, F. Li, J. Zeng, *Nat. Commun.* **2023**, *14*, 474.
[61] J. Wu, X. Wang, H. Li, F. Wang, Y. Hu, *Nano Energy* **2019**, *63*, 103864.
[62] L. Wang, Y. Wan, Y. Ding, Y. Niu, Y. Xiong, X. Wu, H. Xu, *Nanoscale* **2017**, *9*, 4090.